Proceedings of the ASME 2016 Dynamic Systems and Control Conference
DSCC2016
October 12-14, 2016, Minneapolis, Minnesota, USA

DSCC2016-9782

EXPERIMENTAL VALIDATION OF GRAPH-BASED MODELING FOR THERMAL FLUID POWER FLOW SYSTEMS

Justin P. Koeln **Matthew A. Williams** **Herschel C. Pangborn** **Andrew G. Alleyne**
Mechanical Science and Engineering Department
University of Illinois at Urbana-Champaign
Urbana, IL 61801, USA
koeln2@illinois.edu mwillms4@illinois.edu pangbor2@illinois.edu alleyne@illinois.edu

ABSTRACT

Model-based control design has the ability to meet the strict closed-loop control requirements imposed by the rising performance and efficiency demands on modern engineering systems. While many modeling frameworks develop control-oriented models based on the underlying physics of the system, most are energy domain specific and do not facilitate the integration of models across energy domains or dynamic time-scales. This paper presents a graph-based modeling framework, derived from the conservation of mass and energy, which captures the structure and interconnections in the system. Subsequently, these models can be used in model-based control frameworks for thermal management. This framework is energy-domain independent and inherently captures the exchange of power among different energy domains. A thermal fluid experimental system demonstrates the formulation of the graph-based models and the ability to capture the hydrodynamic and thermodynamic behaviors of a physical system.

I. INTRODUCTION

Conventional approaches to modeling and control of complex systems-of-systems are often limited to decentralized high-fidelity modeling and robust, low performance proportional-integral and logic-based control [1]. Holistic modeling, analysis, and control design is inhibited by the complexity and size of the systems, especially when dynamics evolve over a wide range of timescales and energy domains. Vehicle systems in particular consist of multiple systems including electrical, thermal, fuel, hydraulic, pneumatic, and mechanical. They are also characterized by significant interactions across energy domain boundaries over timescales ranging from sub-milliseconds in the electrical system to minutes or hours in the thermal system. While each of these systems may have significantly different dynamics governed by their individual energy domains, each system satisfies conservation equations, such as the conservation of mass and energy. Thus, these systems can be unified under the umbrella of “power flow systems" wherein each system satisfies conservation of energy and the coupling between systems is characterized by the exchange of power.

As the demands for performance and efficiency of these systems continues to increase, it is imperative to optimize the generation, storage, distribution, and consumption of power through advanced control strategies. To this effect, extensive research efforts have focused on these aspects of power control for many types of systems that fall within the category of power flow systems. Examples include microgrids [2], water distribution networks [3], chemical process networks [4], hydraulic hybrid vehicles [5], and thermal energy systems [6].

As the complexity of systems increases, developing, analyzing, and validating control designs must be conducted in simulation prior to application to the physical system. Due to the complexity of the systems and corresponding models, modular, toolbox-based modeling frameworks are often developed. Examples in the fields of building and vehicle energy management include the Thermosys™ [7] toolbox for modeling air-conditioning and refrigeration systems, the ATTMO [8] toolbox for modeling aircraft vapor cycle systems, and the PowerFlow toolbox for holistic aircraft power system modeling [9]. Each of these toolboxes consists of individual component models that can be interconnected to form complete systems. This modularity allows for individual sizing and validation of components and permits a wide range of system configurations and sizes to be implemented in simulation.

To validate both modeling toolboxes and control approaches, experimental testbed systems have been developed across a range of application areas. Examples include the vapor compression refrigeration testbeds of [7] and [10], the hydraulic hybrid vehicle testbed of [5], the aircraft fuel thermal

management system testbed of [11], and the shipboard chilled water distribution system testbed of [12].

A graph-based approach to modeling power flow systems can be particularly convenient for facilitating model-based control design, as shown in [13] for building thermal dynamics, [14] for process systems, and [11] and [15] for vehicle energy management systems. However, control approaches using graph-based modeling have been primarily implemented in simulation. In order to prove the efficacy of these control techniques for real-world implementation, it is first essential to demonstrate experimentally that graph-based modeling approaches can accurately capture the dynamics of power flow systems.

The objective of this paper is to demonstrate the value and applicability of the graph-based modeling framework for thermal fluid systems through experimental validation. A modular, and readily expandable experimental testbed is presented and used to showcase the ability of a graph-based framework to capture the dynamics of a thermal fluid system. Furthermore, it is shown that a graph-based modeling approach provides a single flexible framework in which power flow dynamics can be represented using nonlinear or linear relationships.

The remainder of the paper is organized as follows. Section II presents the generic graph-based modeling framework, followed by specific formulations, derived from mass conservation and thermal energy conservation, applicable to the current experimental system. First-principles and empirical models are developed for select fluid thermal system components in Section III, which demonstrates the graph-based viewpoint and modeling procedure. Details of the experimental system are provided in Section IV, the specific hydraulic and thermal graphs for this system are developed in Section V, and experimental validation of the nonlinear and linearized graph-based models is presented in Section VI. The value of the graph-based modeling framework is discussed in Section VII with conclusions and future extensions provided in Section VIII.

II. GRAPH-BASED SYSTEM MODELING

The dynamics of the specific systems discussed in the literature from Section I all satisfy conservation equations for mass and energy. Elements of these systems such as liquid tanks, hydraulic pressure vessels, and hydraulic cylinders storing mass, which is transported between storage elements via fuel and hydraulic lines. Similarly, elements such as heat exchangers, cockpits/cabins, fluid tanks, and phase-change thermal storage devices store thermal energy, which is transported via conduction, convection, radiation, or mass transport driven by compressors, pumps, and fans. For electrical systems, elements such as batteries and capacitors store electrical energy with transport along electrical wire controlled by switches.

Regardless of the conserved quantity (mass or energy) or the energy domain (electrical, thermal, or hydraulic), a graph-based modeling framework inherently captures the storage and transport of the conserved quantity. When modeling a system as a graph, capacitive elements that store energy, or mass, are represented as vertices and the paths for the transport of energy, or mass, between storage elements are represented as edges. Fig. 1 shows an example of such a graph used to identify important aspects of graph-based modeling. While this graph-based modeling framework is equally applicable to both mass and energy conservation, for the general discussion of graph-based modeling, vertices will store energy and power will flow along edges.

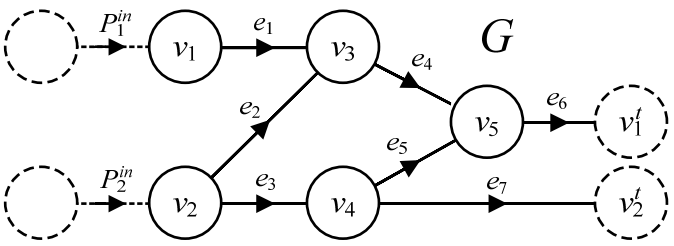

Fig. 1. Notional system graph used to demonstrate graph-based modeling framework and key attributes.

Generic Graph Formulation

Let the oriented graph $G=(V,E)$ represent the structure of energy storage and power flow throughout the system $\mathbf{S}$, with the set of N_v vertices $V=\{v_i\}$, $i\in[1,N_v]$ and the set of N_e edges $E=\{e_j\}$, $j\in[1,N_e]$. The orientated edge e_j represents the direction of positive power flow from the tail vertex v_j^{tail} to the head vertex v_j^{head}. Each edge has an associated power flow P_j. For each vertex v_i, the set of edges directed toward the vertex is $E_i^{in}=\{e_j \mid v_j^{head}=v_i\}$ and the set of edges directed from the vertex is $E_i^{out}=\{e_j \mid v_j^{tail}=v_i\}$. Additionally, each vertex v_i has an associated state x_i representing the amount of stored energy. Thus the dynamics of each vertex satisfy the energy conservation equation

$$C_i\dot{x}_i=\sum_{e_j\in E_i^{in}}P_j-\sum_{e_j\in E_i^{out}}P_j, \tag{1}$$

where C_i is the energy storage capacitance of the vertex v_i. Within the proposed graph-based modeling framework, the power flows P_j are constrained to be a function of an associated input u_j and the states of the tail x_j^{tail} and head x_j^{head} vertices where

$$P_j=f_j\left(x_j^{tail},x_j^{head},u_j\right). \tag{2}$$

In addition to the power flows between vertices within the graph, Fig. 1 shows examples of power flows P_1^{in} and P_2^{in} entering the system along dashed edges. These power flows are treated as disturbances to the system and may come from neighboring systems or the surrounding environment. The sink

vertices v_1^t and v_2^t, and the edges directed toward these vertices, are part of the graph G but the states of these vertices x_1^t and x_2^t are not states of the system $\mathbf{S}$. Instead, these states represent states of neighboring systems or the surrounding environment and are treated as disturbances to the system $\mathbf{S}$.

The structure of this system is captured by the incidence matrix $M = \left[m_{ij} \right]$ [16] where

$$m_{ij} = \begin{Bmatrix} +1 & v_i \text{ is the tail of } e_j \\ -1 & v_i \text{ is the head of } e_j \\ 0 & \text{else} \end{Bmatrix}. \quad (3)$$

Using this incidence matrix and the energy conservation dynamic for each vertex (1), the system dynamics are

$$\mathbf{S}: \begin{bmatrix} C\dot{x} \\ \dot{x}^t \end{bmatrix} = -MP + \begin{bmatrix} D \\ 0 \end{bmatrix} P^{in}, \quad (4)$$

where $x = \left[x_i \right]$ are the states of all the dynamic vertices, $x^t = \left[x_i^t \right]$ are the states of the sink vertices, $P = \left[P_i \right]$ are the power flows along the edges of G, $P^{in} = \left[P_i^{in} \right]$ are the source power flows entering $\mathbf{S}$, $C = diag\left(\left[C_i \right] \right)$ is a diagonal matrix of the capacitances of each vertex, and $D = \left[d_{ij} \right]$ is a matrix where

$$d_{ij} = \begin{Bmatrix} 1 & v_i \text{ is the head of } P_j^{in} \\ 0 & \text{else} \end{Bmatrix}. \quad (5)$$

As previously discussed, since x_i^t are disturbances to the system, not states, M is partitioned as $M = \begin{bmatrix} \bar{M}^T & \underline{M}^T \end{bmatrix}^T$, resulting in

$$\mathbf{S}: C\dot{x} = -\bar{M}P + DP^{in}. \quad (6)$$

Finally, the vector of power flows in $\mathbf{S}$ is represented as

$$P = F\left(x, x^t, u \right), \quad (7)$$

where $F\left(x, x^t, u \right) = \left[f_j \left(x_j^{tail}, x_j^{head}, u_j \right) \right]$, resulting in the nonlinear dynamics for $\mathbf{S}$:

$$\mathbf{S}: C\dot{x} = -\bar{M}F\left(x, x^t, u \right) + DP^{in}. \quad (8)$$

Multi-graph System Representation

The previous section described the graph-based modeling framework in terms conservation of energy and the flow of power. Many real-world systems are governed by both conservation of mass and conservation of energy. Thus the dynamics of these systems may be represented as two coupled graphs, as shown in Fig. 2. The first graph, denoted G^m in Fig. 2, is governed by mass conservation laws, while the second graph, denoted G^e, is governed by energy conservation laws. As with many engineering analyses, for this work, it is assumed that the coupling between these two graphs is limited to the unidirectional influence of mass dynamics on the energy dynamics.

For notation purposes, a superscript m is used to denote the mass conservation system dynamics. Additionally, instead of power flows P_j, the edges in graph G^m represent mass flow rates, $\dot{m}_j$, and the states represent pressures p_i (not to be confused with the power flows P_j). Thus, from (6), the dynamics of the mass conservation system $\mathbf{S}^m$ become

$$\mathbf{S}^m: C^m \dot{p} = -\bar{M}^m \dot{m} + D^m \dot{m}^{in}, \quad (9)$$

where $\dot{m} = F^m\left(p, p^t, u \right)$ is a vector of the individual equations $\dot{m}_j = f_j^m \left(p_j^{tail}, p_j^{head}, u_j \right)$ expressing the relationships between mass flow rate, the neighboring pressures, and a corresponding actuator input.

Similarly, a superscript t denotes the thermal energy conservation system dynamics. Here, the power flows P_j represent thermal power flow, and the states represent temperature T_i. Thus, from (6), the dynamics of the thermal energy conservation system $\mathbf{S}^t$ become

$$\mathbf{S}^t: C^t \dot{T} = -\bar{M}^t P + D^t P^{in}, \quad (10)$$

where $P = F^t\left(T, T^t, \dot{m}^t \right)$ is a vector of the individual equations $P_j = f_j^t \left(T_j^{tail}, T_j^{head}, \dot{m}_j^t \right)$. Note that the mass flow rates from G^m become inputs to the thermal system. The edges in G^m may not align one-to-one with the edges in G^t. Therefore, the mass flow rates from G^m are mapped to the input mass flow rate to G^t by $\dot{m}^t = Z\dot{m}$, where $Z \in \mathbb{R}^{N_e^t \times N_e^m}$.

Finally, the actuators, which affect the mass flow rates in $\mathbf{S}^m$, may have decoupled actuator dynamics, as shown in Fig. 2. The i^{th} actuator is assumed to have the general nonlinear dynamic

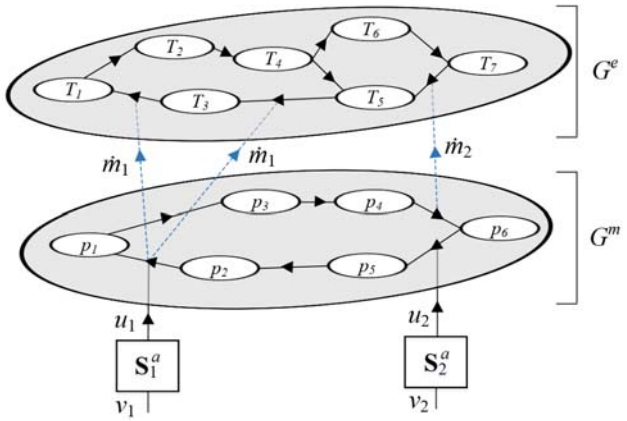

Fig. 2. Two-level graph showing the interconnection between a mass conservation graph (bottom) and an energy conservation graph (top) with mass dynamics affecting the energy conservation graph.

$$\mathbf{S}_i^a:\ \begin{aligned} \dot{w}_i &= g_i\left(w_i, v_i\right), \\ u_i &= h_i\left(w_i, v_i\right), \end{aligned} \tag{11}$$

where v_i is the manipulated input to the actuator and u_i is the output of the actuator which affects the mass flow dynamics.

III. CONSERVATION-BASED MODELING

The generic graph-based modeling framework presented in the previous section can be used to capture the dynamics of a wide variety of systems. Many systems are comprised of a heterogeneous mix of components. Often it is useful to model components individually and then combine the individual component models to build up an entire system model.

Graph-based modeling relies on the assumption of lumped parameters. For example, the mass stored in a fluid volume is captured by a single representative pressure while the thermal energy stored in a thermal mass is captured by a single representative temperature. The first step to modeling a component is to identify the capacitive elements within the component and corresponding state values that represent the stored quantities. It is recommended that each component be represented with as few vertices as necessary to capture the relevant dynamics. If additional fidelity is needed, the component model can easily be further discretized with additional vertices and states. Once the vertices are identified, it is often a simple matter to determine the possible paths by which mass or energy can enter or exit that storage element and to represent these paths as edges. In order to keep models simple, it is suggested that only dominant power flows are represented as edges. If, during validation of the graph, it becomes apparent that a significant power flow was omitted from the graph, such as heat loss to ambient, edges can easily be added to improve the accuracy of the model.

For demonstration purposes, the remainder of this section develops a set of models for components often found in thermal fluid systems. These components include a fluid reservoir, a flow split/junction, a pump, a pipe, a cold plate heat exchanger, and a liquid-to-liquid brazed plate heat exchanger. Fig. 3 shows the mass conservation and thermal energy conservation graphs for each component. Dashed lines, indicating disturbances to each component, consist of variables determined by neighboring components. For example, the reservoir and flow split/junction only calculate their own pressure based on mass flow rates determined by neighboring components. However, the pump and heat exchangers calculate their own outlet pressure and inlet mass flow rate based on the upstream pressure and downstream mass flow rate. The following details the modeling of these components based on their graph frameworks from Fig. 3.

Mass Conservation

All pressure dynamics are derived from the mass conservation equation $\dot{M} = \dot{m}_1 - \dot{m}_2$, where $\dot{M}$ is the rate-of-change of fluid mass stored in the component and $\dot{m}_1$ and $\dot{m}_2$ are the total flow rates into and out of the component. For

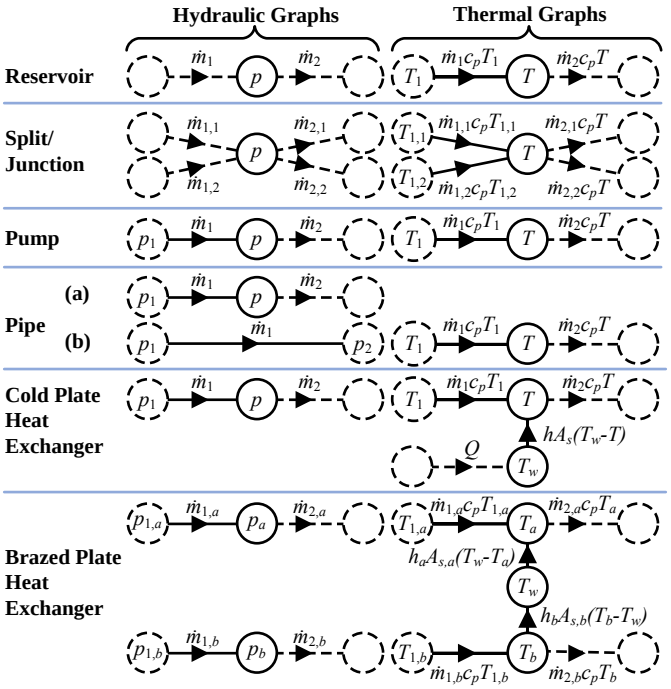

Fig. 3. Hydraulic and thermal graphs for individual components.

components with a fixed volume V, the change in mass stored in a component is based on the change in density ρ of the fluid as a function of pressure p. Thus $\dot{M} = V\dot{\rho} = V\left(\partial\rho/\partial p\right)\dot{p}$. Noting that the change in density with pressure is based on the bulk modulus of the fluid E, where $\partial\rho/\partial p = \rho/E$, the mass conservation equation provides a dynamic equation for pressure within the component,

$$V\frac{\rho}{E}\dot{p} = \dot{m}_1 - \dot{m}_2 . \tag{12}$$

Currently, the only component without a fixed volume is the reservoir. The reservoir has a constant cross sectional area $A_{c,r}$ with a liquid height h_r. The top of the reservoir is subject to ambient air pressure p_{amb}. Fluid flows into and out of the reservoir from the bottom with flow rates $\dot{m}_1$ and $\dot{m}_2$. The mass stored in the reservoir M_r changes as a function of these flow rates: $\dot{M}_r = \dot{m}_1 - \dot{m}_2$. This dynamic is expressed in terms of the pressure p_r at the bottom of the reservoir using the relationship between mass and liquid height, $M_r = \rho A_{c,r} h_r$, and the relationship for static pressure in a liquid, $p_r = p_{amb} + \rho g h_r$. The resulting pressure dynamic is

$$A_c\dot{p}_r = g\left(\dot{m}_1 - \dot{m}_2\right). \tag{13}$$

Note that the flow split/junction has n inlets and m outlets and thus the inlet and outlet flow rates are calculated as $\dot{m}_1 = \sum_{i=1}^{n}\dot{m}_{1,i}$ and $\dot{m}_2 = \sum_{i=1}^{n}\dot{m}_{2,i}$.

The mass flow rates through pipes and heat exchangers is based on the pressure drop across the component $\Delta p = p_1 - p$ and the height difference between the inlet and outlet flow Δh. Fluid flows through a cross sectional area of A_c, based on tube diameter D, for a length L. Major losses are determined based on the friction factor f and minor losses are modeled using the a minor loss coefficient K_L. Pipes may include the pressure drop effects of various sensors via this minor loss coefficient. With s sensors along the pipe the total minor loss coefficient is $K_L = K_L^{pipe} + \sum_{i=1}^{s} K_L^i$. The resulting equation for the mass flow rate through a pipe or heat exchanger is

$$\dot{m} = \rho A_c \sqrt{\frac{2\left(p_1 - p + \rho g \Delta h\right)}{\rho\left(f\frac{L}{D} + K_L\right)}}. \qquad (14)$$

Note that Fig. 3 shows two forms of pipes. Pipe version (a) is the standard component which calculates a dynamic outlet pressure p and the inlet mass flow rate $\dot{m}_1$. Pipe version (b) only calculates a mass flow rate $\dot{m}$ between two pressures p_1 and p_2, which are determined by neighboring components. Version (b) of the pipe is used at the inlet to the reservoir and flow split/junction, since these components do not calculate their own inlet mass flow rates.

For the brazed plate heat exchangers, there are N_c channels for each fluid, the width of each plate is W, and the spacing between plates is b. Thus when using (14), $A_c = N_c bW$ is the cross sectional area of a single channel multiplied by the number of channels and $D = 4bW/(2b+2W)$ is the hydraulic diameter of a single channel.

The mass flow rate calculation for the pump is a function of the pressure differential across the pump $\Delta p_p = p - p_1$ and the pump speed ω. The mass flow rate is $\dot{m} = \rho A_c u_m$, where u_m is the mean fluid velocity. From conservation of mechanical energy the fluid velocity is $u_m = \sqrt{2g\left(H - \Delta p_p/(\rho g)\right)}$, where $H = H\left(\Delta p_p, \omega\right)$ is the pump head. Thus the mass flow rate through the pump is

$$\dot{m} = \rho A_c \sqrt{2g\left(H - \frac{\Delta p_p}{\rho g}\right)}. \qquad (15)$$

Fig. 4 shows an example of a experimentally obtained pump head map with $H = k_1 + k_2 \Delta p_p + k_3 \omega$.

Thermal Energy Conservation

All temperature dynamics are derived from the thermal energy conservation equation $\dot{E}_{st} = P_1 - P_2$, where $E_{st} = Mc_pT$ is the stored thermal energy and P_1 and P_2 are the rate of thermal energy entering or exiting the storage element. In

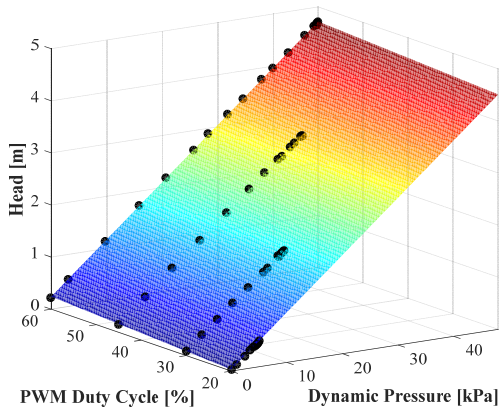

Fig. 4. Example pump head map.

general, $\dot{E}_{st} = \dot{M}c_pT + Mc_p\dot{T}$, which accounts for the change in thermal energy associated with the change of mass M. The first term is important to consider for components, such as the reservoir, which may undergo a significant change in mass. However, for most components, $\dot{E}_{st} \cong Mc_p\dot{T} = \rho V c_p \dot{T}$. For the reservoir, pump, and pipes, the power flow due to fluid flow into the component P_1 is $P_1 = \dot{m}_1 c_p T_1$ and the power flow out of the component P_2 is $P_2 = \dot{m}_2 c_p T$. The lumped temperature represents the fluid temperature at the outlet of the component with the dynamic

$$\rho V c_p \dot{T} = \dot{m}_1 c_p T_1 - \dot{m}_2 c_p T. \qquad (16)$$

For the flow split/junction the temperature dynamic is similar with

$$\rho V c_p \dot{T} = \sum_{i=1}^{n} \dot{m}_{1,i} c_p T_{1,i} - \sum_{i=1}^{m} \dot{m}_{2,i} c_p T. \qquad (17)$$

The cold plate heat exchanger has an additional temperature dynamic capturing the thermal capacitance of the wall. With a heat load of Q, the cold plate wall temperature dynamic is

$$M_w c_{p,w} \dot{T}_w = Q - hA_s\left(T_w - T\right), \qquad (18)$$

where h is the heat transfer coefficient and A_s is the convective surface area. The heat transfer coefficient is calculated based on a Nusselt number, $Nu = hD/k$, of $Nu = 3.66$ for laminar flow or the Gnielinski equation [17]

$$Nu = \frac{(f/8)(\mathrm{Re}-1000)\mathrm{Pr}}{1+12.7(f/8)^{1/2}\left(\mathrm{Pr}^{2/3}-1\right)}, \qquad (19)$$

for turbulent flow. With the additional convective heat flow, the fluid outlet temperature dynamic for the cold plate is

$$\rho V c_p \dot{T} = \dot{m}_1 c_p T_1 + hA_s\left(T_w - T\right) - \dot{m}_2 c_p T. \qquad (20)$$

Finally, the brazed plate heat exchanger is modeled similarly to the cold plate heat exchanger where the heat load Q is replaced by secondary fluid flow. The plates of the heat exchanger are assumed to be at a uniform lumped temperature T_w with the dynamic

$$M_w c_{p,w} \dot{T}_w = h_b A_{s,b} \left(T_b - T_w \right) - h_a A_{s,a} \left(T_w - T_a \right), \qquad (21)$$

where subscripts a and b denote the primary and secondary fluids channels, M_w is the mass of a single plate, and A_s is the convective surface area for a single channel. For the plate heat exchangers, the heat transfer coefficient is based on the empirical results from [18], where

$$Nu = 0.277 \, \mathrm{Re}^{0.766} \, \mathrm{Pr}^{0.333}. \qquad (22)$$

Note that all components are assumed to be adiabatic and do not exchange heat with the surroundings. If this heat loss needed to be considered, the component graphs in Fig. 3 could easily be modified with an additional edge directed to a new vertex with a corresponding state equal to the ambient air temperature.

In general, the equations used to represent the hydraulic and thermodynamic behaviors in this Section have a nonlinear form but satisfy the generic conservation and power flow relationships from (1) and (2). For control design in particular, it is often useful to use a linear representation of the system dynamics. One of the key benefits of a graph-based approach is that this linearization can be performed for each power flow relationship individually. Thus, when linearized, (2) becomes

$$\Delta P_j = a_j \Delta x_j^{tail} + b_j \Delta x_j^{head} + c_j \Delta u_j \qquad (23)$$

where the Δ denote the deviation from the linearization point.

IV. EXPERIMENTAL SYSTEM DESCRIPTION

The following experimental system is used to demonstrate the applicability and validity of the graph-based modeling framework presented in the previous section. This experimental testbed was developed to emulate features of power flow systems while being rapidly reconfigurable to allow for numerous system architectures. Currently, the experimental system focuses on the thermal and hydrodynamic energy domains, with future work concentrating on expansion to the electrical domain. This experimental system is intended to serve as preliminary validation hardware for advanced control architectures, such as the hierarchical model predictive control frameworks proposed in [15], [20].

Overall System

Fig. 5 shows the testbed with a sample system configuration along with the corresponding system schematic. The slatted design of the testbed allows components to be placed in arbitrary horizontal or vertical positions, similar to a breadboard for electrical circuits. The working fluid is an equal parts mixture of propylene glycol and water. Components use standard G1/4 threaded barbs and are connected via flexible tubing. Sensors and pumps are connected to a National Instruments CompactDAQ via custom USB plug interfaces.

Individual Components

Table 1 and Fig. 6 contain specifications and images of the components currently included in the testbed.

Centrifugal pumps are the primary fluid movers in the system. Speed is controlled via a PWM duty cycle with <20%

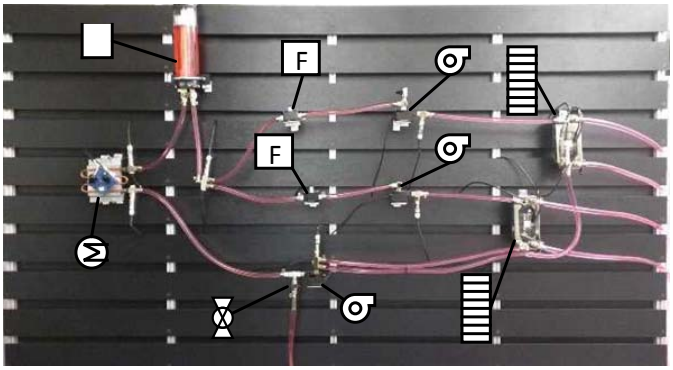

(a) Experimental System

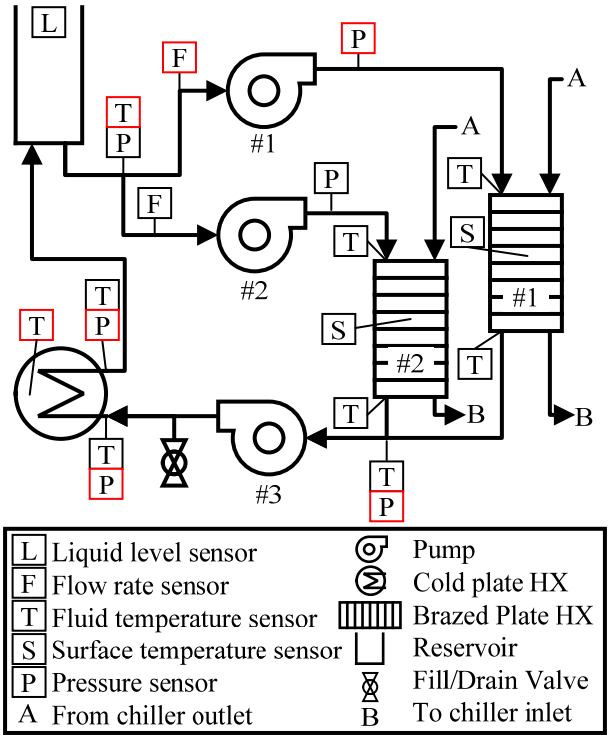

(b) System Schematic (red sensors are plotted in Section VI)

Fig. 5. Candidate thermal power architecture for simulation and experimental validation.

being a constant 1300RPM, 60% and above being 4500RPM, and a linear trend between. Peak power consumption of the pumps is 20W with a peak efficiency of 35%.

Liquid-to-liquid brazed plate heat exchangers (HX) allow for the transfer of heat among various fluid loops in either a parallel-flow or counter-flow configuration.

The cold plate heat exchanger consists of a 25Ω resistive heater, capable of 2kW peak power output, mounted to a steel cold plate that has copper tubing passing through. The heater is connected to a solid-state relay which allows for 0-100% power output using the 208VAC wall power supply.

The reservoir acts as a thermal storage element. A liquid level sensor inside the reservoir allows for the calculation of

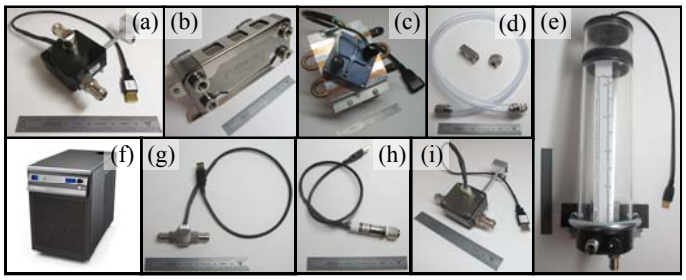

Fig. 6. Individual components from Table 1 with a 6" ruler for scale.

Table 1. Component descriptions

Component	*Number*	*Details*
(a) Pump	8	• Swiftech MCP35X • 12VDC, 1.5A max, PWM ctrl. • 4.4 m max head • 17.5 LPM max flow
(b) Brazed Plate HX	4	• Koolance HXP-193 • 12 plates • 4.0 kW @ 5 LPM and 20°C inlet temp. diff.
(c) Cold Plate HX	4	• Ohmite CP4 with TAP2000 thick film resistor • 0.018 °C/W thermal resistance • 2000W
(d) Pipe	-	• Koolance HOS-13CL • Clear PVC • 13mm x 16mm
(e) Reservoir	4	• Koolance 80x240mm • Acrylic • 8" eTape Liquid Level Sensor
(f) Chiller	1	• Polyscience 6000 Series • Up to 2900W @ 20°C • -10°C to +70°C
(g) Temp. Sensor	16	• Koolance SEN-AP008B • 10K ohm thermistor
(h) Pressure. Sensor	7	• Measurement Specialties US300 • 0 – 100kPa gauge
(i) Flow Rate Sensor	8	• Aqua Computer High Flow • 0.5 – 25 LPM

the liquid mass and therefore thermal capacitance of the reservoir.

A 1.5HP (1.12kW) industrial chiller acts as a heat sink (e.g. a vapor compression system). With variable temperature control from -10°C to 70°C, the chiller can emulate a wide range of source and sink temperatures.

Temperature and pressure sensors utilize G1/4 threads and integrate seamlessly into the tube junctions. As such, limited pressure drops are incurred due to the inclusion of these sensors within the system. Similarly, mass flow sensors use G1/4 threads to attach in line with pipes but the paddlewheel-based design does introduce significant pressure drops.

V. GRAPH-BASED SYSTEM REPRESENTATION

To represent an entire system as a graph, the individual component models from Section III are simply connected to reflect the given system architecture. The following subsections demonstrate how the conservation-based modeling equations from Section III are assembled into the generic graph-based models from Section II for the example experimental system configuration.

Mass Conservation System

Based on the individual component graphs from Fig. 3, the example system configuration shown in Fig. 5 is modeled using the graph-based framework with the resulting hydraulic and thermal graphs shown in Fig. 7. The fluid system is a closed system where fluid mass does not enter or exit the system. Thus (6) reduces to

$$C^m \dot{p} = -\bar{M}^m \dot{m}, \tag{24}$$

where $C^m = diag\left(\left[C_i^m\right]\right)$ and $C_i^m = V\rho/E$ for all vertices except the reservoir where $C_i^m = A_c/g$. The mass flow rate function $\dot{m}_j = f_j^m\left(p_j^{tail}, p_j^{head}, u_j\right)$ equals (14) for the pipes and heat exchangers and (15) for the pumps. To simplify the graph equations, a constant fluid density of $\rho = 1041 kg/m^3$ is used. For the linear graph results in the following section, (14) and (15) are linearized about a nominal operating condition (50% pump PWM duty cycles and 400W heat load into the cold plate).

Thermal Energy Conservation System

Fig. 7 also shows the thermal graph for the experimental system. On the left side the dashed edge indicates the heat generated by the electrical heater entering the cold plate heat exchanger, which is treated as a disturbance to the system. Similarly, on the right side of the graph the dashed edges denote source and sink heat flows from and to the chiller, which is treated as an infinite source/sink of thermal energy. Thus in (10),

$$P^{in} = \begin{bmatrix} Q & \dot{m}_{1,b} c_p T_{1,b} & \dot{m}_{2,b} c_p T_{2,b} \end{bmatrix}^T, \tag{25}$$

where Q is the heat load to the cold plate heat exchanger and $\dot{m}_{1,b}$ and $\dot{m}_{2,b}$ are the secondary fluid flow rates through heatexchangers 1 and 2 with corresponding inlet temperatures $T_{1,b}$ and $T_{2,b}$ set by the chiller. The thermal capacitances C_i^t are $C_i^t = \rho V c_p$ for all fluid temperatures and $C_i^t = M_w c_{p,w}$ for all heat exchanger wall temperatures. The thermal power flow function $P_j = f_j^t\left(T_j^{tail}, T_j^{head}, \dot{m}_j\right)$ equals $P_j = \dot{m}_j c_p T_j^{tail}$ for all thermal power flow due to fluid flow and $P_j = h_j A_{s,j}\left(T_j^{tail} - T_j^{head}\right)$ for convective thermal power flows in the heat exchangers. To simplify the graph system equations, a constant fluid specific heat of $c_p = 3500 J/\left(kg \cdot K\right)$ is used. Additionally, to reduce the complexity of the power flow equations, the heat transfer correlation from (19) is approximated, with (18) and (20) using $h = \alpha_1 + \alpha_2 \dot{m} T$, where $\alpha_1 = -309$ and $\alpha_2 = 1253$ for the cold plate heat exchanger.

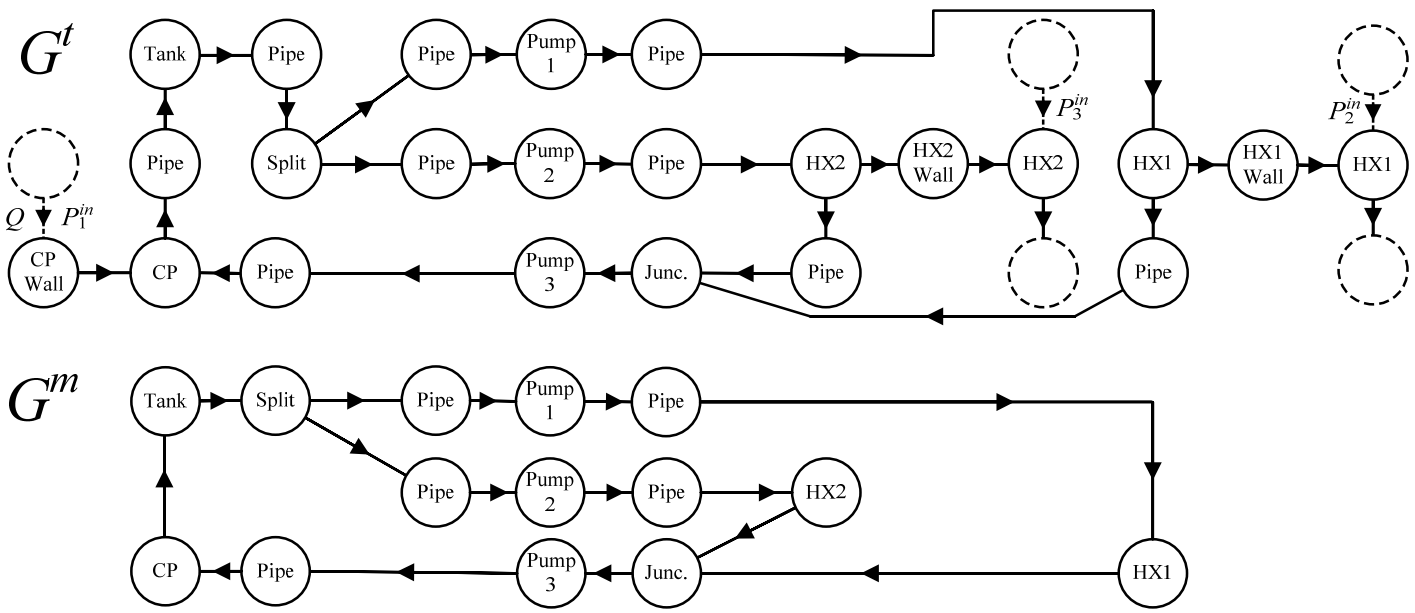

Fig. 7. Hydraulic and thermal graphs for the example experimental system configuration.

Similarly, the heat transfer correlation from (22) for the brazed plate heat exchanger is approximated, and (21) uses $\alpha_1 = 2572$ and $\alpha_2 = 1136$. While these approximations are used successfully within the range of operating conditions seen in the current experimental systems, the nonlinear (19) and (22) may be used over wider ranges of conditions.

VI. MODEL VALIDATION

In this section, the graph-based modeling approach of Section V is validated by comparison of experimental data from the testbed of Section IV to both nonlinear and linear graph-based models, using the configuration shown in Fig. 5. Sensors labeled in red are used in the generation of the validation plots. Separate experimental tests are used to validate the hydrodynamic and thermodynamic domains so that each is validated under excitation on an appropriate timescale (i.e., the hydrodynamics are validated using rapid steps in pump speed, while the significantly slower thermodynamics are validated with slower steps in pump speed and heat load).

Hydrodynamic Validation

Fig. 8 shows the pump input sequence used to validate the hydrodynamics of the models, where the pump numbering follows from that of Fig. 5. Fig. 9 shows a subset of the measured outputs from the testbed (labeled as "Experiment"), as well as the graph-based models (labeled as "Nonlinear Graph" and "Linear Graph"). From Fig. 9, one can confirm that mass flow rates and pressures at multiple locations in the fluid loop coincide closely between the models and experimental data, and that a linear graph is capable of capturing the behavior of the system over these operating conditions.

Thermodynamic Validation

Fig. 10 shows a sequence of pump inputs and heat load to the cold plate wall used to validate the thermodynamics of the models. From Fig. 11, one can confirm that temperature and power flows at multiple locations in the fluid loop coincide closely between the models and experimental data, and are nearly identical between the nonlinear and linear graphs. Discrepancies between the graph-based models and the experimental data are likely due to imperfect pump maps, unmodeled friction/losses, and measurement/calibration error. While these models could be improved, at the cost of increased complexity, the accuracy of the models is sufficient for future closed-loop control purposes.

VII. VALUE OF GRAPH-BASED APPROACH

The results in this paper represent a preliminary demonstration of the capabilities of graph-based modeling. Conceptualizing and modeling a system based on the underlying structure of mass and energy transport between storage elements provides numerous benefits. First, when viewed as a graph, systems of different energy domains look and behave identically. Energy, and/or mass, is transported along edges and stored at the vertices, regardless of whether the vertex state represents a temperature, a pressure, or a voltage. This unifying framework natively captures the interactions between energy domains and thus facilitates system-wide design, analysis, and control.

The second benefit of a graph-based approach comes from the modularity. Vertices and edges are all modeled individually. This allows for rapid development of complex systems with many vertices and edges through the combination of components modeled individually (such as those shown in Fig 3). From this modularity, alternative system configurations can be rapidly evaluated through the rearrangement of components or the addition/subtraction of various edges and vertices. Along these lines, if the overall model validity is not sufficient for the intended purposes of the model, additional fidelity can be

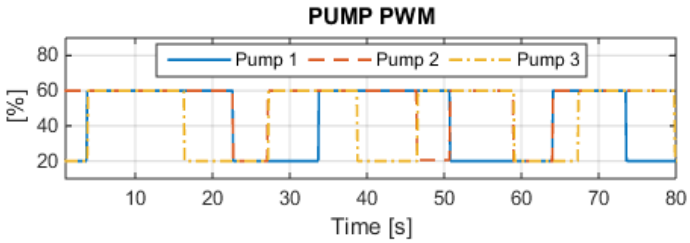

Fig. 8. Pump PWM inputs for hydrodynamic validation.

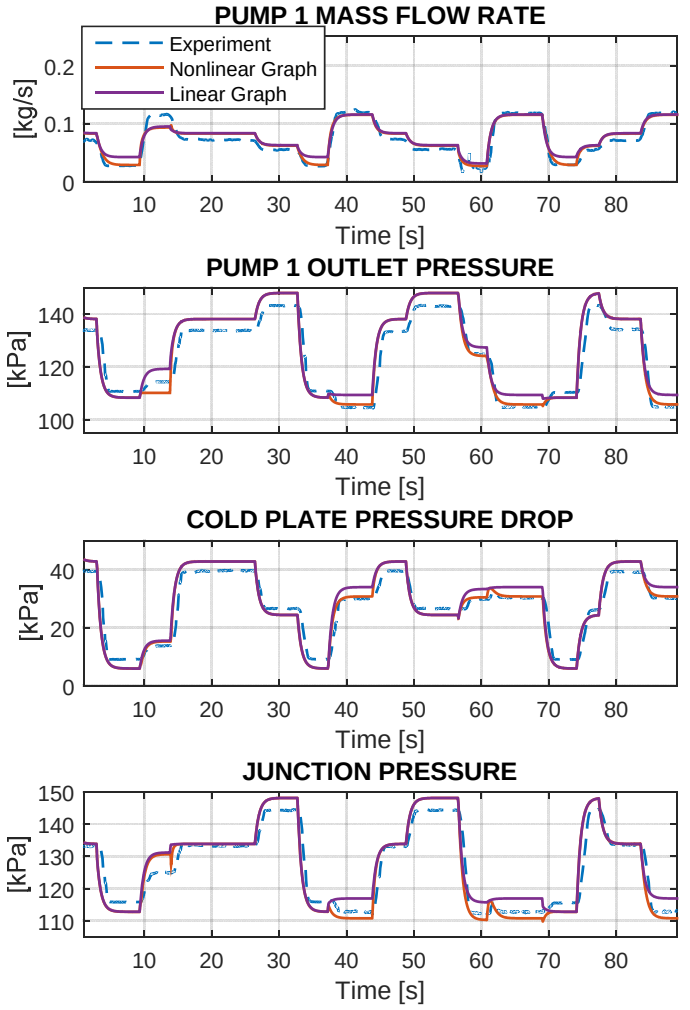

Fig. 9. Selected outputs for hydrodynamic validation.

easily added through the discretization of components captured by additional vertices and edges in the graph.

An additional benefit comes from the flexibility of a graph-based modeling framework. The majority of the system specific behaviors are captured by the edge power flow equation (2). The general, nonlinear form of this equation allows for a wide variety of power flow relationships to be captured within a single framework. While the general form may be nonlinear, (2) may be easily restricted to specific forms, such as input affine, bilinear, or linear, to best suit the needs of the modeling and control efforts.

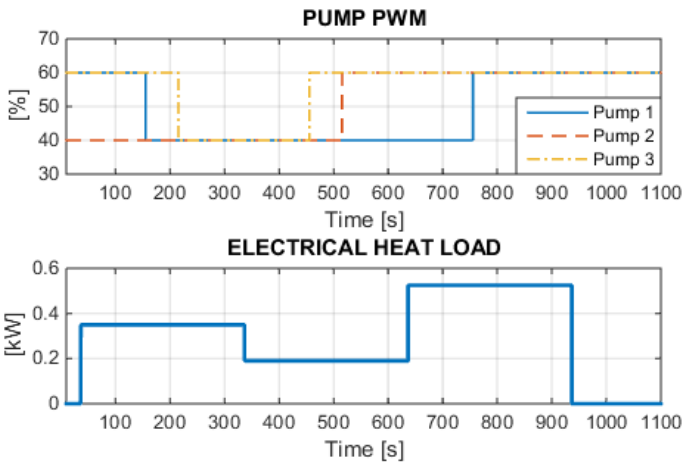

Fig. 10. Pump and heater inputs for thermodynamic validation.

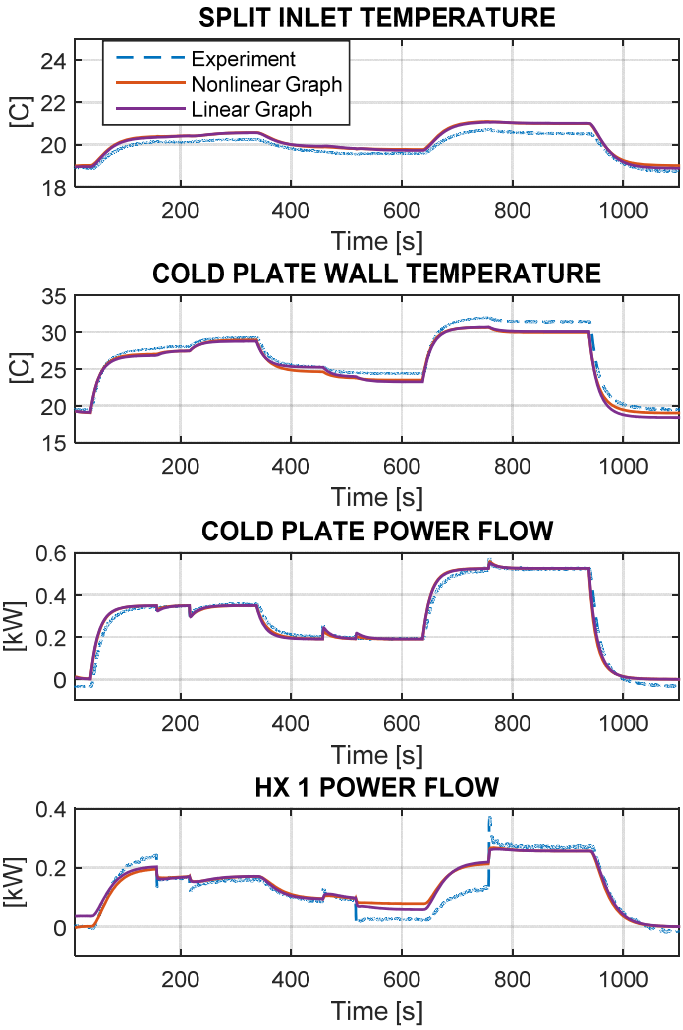

Fig. 11. Selected outputs for thermodynamic validation.

Finally, as is preliminarily demonstrated in [15], [20], the graph-based framework facilitates model-based control design and is especially well suited to decentralized, distributed, and hierarchical control designs where the control structure should be designed based on the structure of the system.

VIII. CONCLUSIONS

This paper presents the development and experimental validation of a graph-based modeling framework for power flow systems. Graphs based on conservation of mass and energy are derived where vertices represent the storage elements and edges capture the transport structure of mass and energy throughout the system. A thermal fluid experimental system is used to demonstrate and validate the proposed modeling framework. Results show that graphs are capable of capturing the steady-state and dynamic behavior of a physical system. Based on these promising results, future work will focus on expansion of the experimental system and the modeling framework to additional energy domains, the development of control structures based on the graph models, and the assessment of these control structures on the experimental system.

ACKNOWLEDGMENTS

This material is based upon work supported by the National Science Foundation Graduate Research Fellowship under Grant Number DGE-1144245, and by the National Science Foundation Engineering Research Center for Power Optimization of Electro Thermal Systems (POETS) with cooperative agreement EEC-1449548.

REFERENCES

[1] B. G. Liptak, *Process Control*, 3rd ed. Chilton, 1995.

[2] J. M. Guerrero, P. C. Loh, T. Lee, and M. Chandorkar, "Advanced Control Architectures for Intelligent Microgrids - Part II: Power Quality, Energy Storage, and AC/DC Microgrids," *IEEE Trans. Ind. Electron.*, 2013.

[3] R. R. Negenborn, A. Sahin, Z. Lukszo, B. De Schutter, and M. Morari, "A non-iterative cascaded predictive control approach for control of irrigation canals," *2009 IEEE Int. Conf. Syst. Man Cybern.*, 2009.

[4] P. D. Christofides, R. Scattolini, D. Muñoz de la Peña, and J. Liu, "Distributed model predictive control: A tutorial review and future research directions," *Comput. Chem. Eng.*, 2013.

[5] T. O. Deppen, "Optimal Energy Use in Mobile Applications with Storage," Ph.D. Dissertation, Dept. Mech. Eng., Univ. Illinois Urbana-Champaign, Urbana, IL, 2013.

[6] N. Jain, J. P. Koeln, S. Sundaram, and A. G. Alleyne, "Partially decentralized control of large-scale variable-refrigerant-flow systems in buildings," *J. Process Control*, 2014.

[7] B. P. Rasmussen, "Dynamic Modeling and Advanced Control of Air Conditioning and Refrigeration Systems," Ph.D. Dissertation, Dept. Mech. Eng., Univ. Illinois Urbana-Champaign, Urbana, IL, 2005.

[8] M. Kania, J. Koeln, and A. Alleyne, "A Dynamic Modeling Toolbox for Air Vehicle Vapor Cycle Systems," *Proc. 2012 SAE Power Syst. Conf.*, 2012.

[9] M. Williams, S. Sridharan, S. Banerjee, C. Mak, C. Pauga, P. Krein, A. Alleyne, A. Jacobi, and S. D. Urso, "PowerFlow : A Toolbox for Modeling and Simulation of Aircraft Systems," *SAE Tech. Pap. 2015-01-2417*, 2015.

[10] A. Puntel, S. Emo, T. E. Michalak, J. Ervin, L. Byrd, V. Tsao, and T. Reitz, "Refrigerant Charge Management and Control for Next-Generation Aircraft Vapor Compression Systems," *SAE Tech. Pap. 2013-01-2241*, 2013.

[11] T. O. Deppen, J. E. Hey, A. G. Alleyne, and T. S. Fisher, "A Model Predictive Framework for Thermal Management of Aircraft," *ASME 2015 Dyn. Syst. Control Conf.*, 2015.

[12] S. K. Srivastava, D. A. Cartes, F. Maturana, F. Ferrese, M. Pekala, M. Zink, R. Meeker, D. Carnahan, R. Staron, D. Scheidt, and K. Huang, "A Control System Test Bed for Demonstration of Distributed Computational Intelligence Applied to Reconfiguring Heterogeneous Systems," *IEEE Instrum. Meas. Mag.*, 2008.

[13] K. L. Moore, T. L. Vincent, F. Lashhab, and C. Liu, "Dynamic Consensus Networks with Application to the Analysis of Building Thermal Processes," *IFAC World Congr.*, 2011.

[14] H. A. Preisig, "A graph-theory-based approach to the analysis of large-scale plants," *Comput. Chem. Eng.*, 2009.

[15] J. P. Koeln, M. A. Williams, and A. G. Alleyne, "Hierarchical Control of Multi-Domain Power Flow in Mobile Systems - Part I: Framework Development and Demonstration," *ASME 2015 Dyn. Syst. Control Conf.*, 2015.

[16] D. B. West, *Introduction to Graph Theory*. Prentice-Hall Inc., 2001.

[17] V. Gnielinski, "New Equations for Heat and Mass-transfer in Turbulent Pipe and Channel Flow," *Int. Chem. Eng.*, 1976.

[18] G. a. Longo and A. Gasparella, "Refrigerant R134a vaporisation heat transfer and pressure drop inside a small brazed plate heat exchanger," *Int. J. Refrig.*, 2007.

[19] Mathworks, "MATLAB/Simulink." Natick, MA, 2015.

[20] M. A. Williams, J. P. Koeln, and A. G. Alleyne, "Hierarchical Control of Multi-Domain Power Flow in Mobile Systems - Part II: Aircraft Application," *ASME 2015 Dyn. Syst. Control Conf.*, 2015.

